International Journal of Impact Engineering 187 (2024) 104911

Contents lists available at ScienceDirect

International Journal of Impact Engineering

journal homepage: www.elsevier.com/locate/ijimpeng

# How rate-based stretchability of soft solids controls fracture morphology in dynamic conical puncture

Bingyang Zhang *, Philip S.L. Anderson

*Department of Evolution, Ecology, and Behavior, School of Integrative Biology, University of Illinois Urbana-Champaign, 505 S. Goodwin Ave., Urbana, 61801, IL, USA*

ARTICLE INFO

*Keywords:*
Puncture
Dynamic
Fracture morphology
Stretchability
Soft solids

ABSTRACT

Puncture is a primary failure mechanism occurring in soft materials and biological tissues when subjected to impact and dynamic deep indentation. While many studies on puncture mechanics focus on the energies and forces associated with fracture, most of the existing models only capture qualitatively experimental measures at low rates and lack strong predictive power for the dynamic crack growth and its material basis. In this work, we employ a novel experimental framework to investigate the relationship between the fracture morphology and rate-based ultimate properties during dynamic puncture of soft and stretchable materials using a conical tool. We discover a scaling relationship between the tangents of the half cusp angles of the undeformed crack and the puncture tool, which gives a constant ratio whose magnitude depends on the combination of the effective strain rate in the material during puncture, and the visco-hyperelastic constitutive response of the material. Our theoretical prediction for the relationship between tensile stretch at failure and strain rate shows a close agreement with the experimental results determined from dynamic conical puncture tests. These findings, combined with two further case studies, confirm the feasibility of postmortem puncture damage characterization as a new tool for extracting ultimate stretch in complex soft biomaterials and biological tissues under dynamic/impact loading.

## 1. Introduction

Puncture of soft materials or tissues via penetration of a sharp, pointed tool is a fundamental failure mechanism in the biological realm [1–9] and bio-related applications [10–21]. Living organisms have evolved a variety of biological weaponry in the form of teeth [1,22], claws [23], spines [3,6], stingers [24] and more [2]. Across a wide span of sizes and operating rates [2,8], these biological puncture tools pierce and cut through target soft tissues with remarkable precision and mechanical performance to achieve a wide range of biological functions such as prey capture, reproduction, and defense [2–4,23,25,26]. A better understanding of the physical principles underlying puncture failure in soft materials and tissues not only has far-reaching implications for the evolution and comparative biomechanics of biological puncture systems; It is also highly instructional for developing more effective bio-inspired medical tools (*e.g.*, needles and probes) [11,27–30] and tissue simulants/phantoms [10,14,31] as simulators to improve the safety and reliability of biomedical operations such as invasive surgery, injection, and biopsy [11,15,32]. Additionally, puncture is widely used in soft materials as an important testing technique for material characterization [19,33,34], design of protective biomaterials [13], and exploration of soft fracture mechanics [35,36] and injury biomechanics [37].

Challenges arising during the investigation of puncture mechanics in soft solids stem from the complex interplay between puncture tool geometries, contact mechanics, and nonlinear constitutive and failure responses associated with large deformation [7,27]. This interplay is ultimately responsible for the initiation and propagation of fracture inside the material substrate during puncture. Previously established energy-based models for puncture have demonstrated their effectiveness in mathematically describing how initial energy investment for puncture failure is divided into energy contributions for fracture, elastic deformation, and friction dissipation [7,18,21,27,38–43]. However, there exists a knowledge gap between the observed unique morphology of puncture fracture surfaces and the underlying fracture mechanics. In particular, current theoretical models for puncture assume a preexisting crack with prescribed geometries. It is not fully understood how the final shape and size of a fracture surface produced by puncture quantitatively depends on the tool geometry, the loading rates, the nonlinear constitutive response, and the ultimate properties of the target material (*e.g.*, stretch at failure). A precise physical description of the material basis governing the crack growth during puncture is of great interest to facilitate the standardization of the puncture testing

* Corresponding author.
*E-mail address:* bzhang53@illinois.edu (B. Zhang).

https://doi.org/10.1016/j.ijimpeng.2024.104911
Received 19 October 2023; Received in revised form 12 January 2024; Accepted 3 February 2024
Available online 6 February 2024

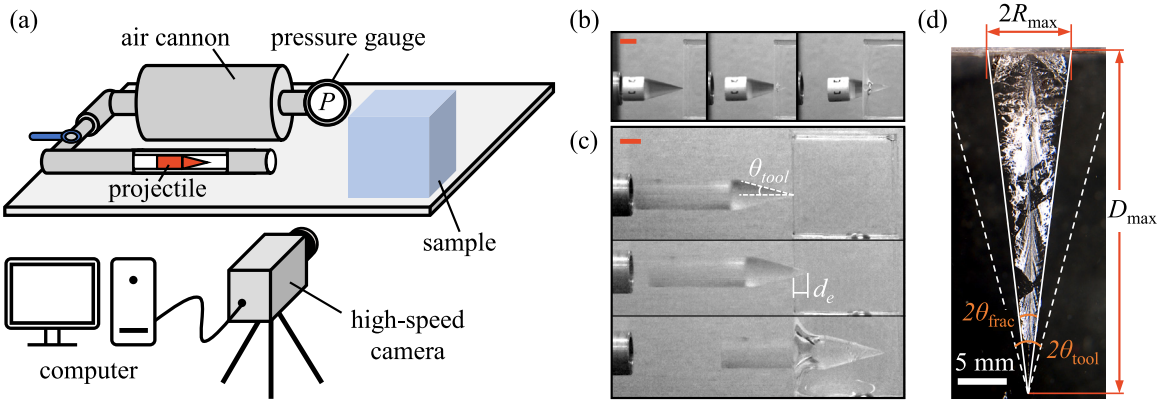


**Fig. 1.** Dynamic conical puncture to characterize fracture morphology. (a) Schematic of the experimental setup. (b) and (c) Still frames from high-speed imaging showing the onset of impact, the maximum indentation ($d_e$), and the maximum penetration ((b): left to right; (c): top to bottom). Puncture rates: (b): $v = 9.4 \pm 0.2$ m/s; (c): $v = 50.3 \pm 1.2$ m/s. Orange scale bars: 10 mm. (d) A representative planar triangular fracture surface obtained at $v = 50.3 \pm 1.2$ m/s to demonstrate the two approaches for characterizing the angular parameters (Eqs. (1) and (2)). The white solid lines outline the edges of the fracture surface. The white dashed lines indicate the cusp angle of the corresponding puncture tool ($2\theta_{tool} = 30°$). Particularly, the fracture surface shown is aligned with the focal plane of the microscope camera.

technique. It holds the potential as a new characterization tool for material failure properties through the examination of injuries and damage morphology in postmortem samples, which can be more effective and cost-efficient than *in operando* characterization approaches, especially in dynamic/ballistic loading scenarios (*e.g.*, Refs. [44–46]).

Previous experimental [21,38,47,48] and computational [18,39,41,42,49] explorations on the size/morphology of puncture fracture were primarily focused on puncture with a cylindrical tool under a quasi-static loading condition. The findings of these studies are insightful and informative for the development of biomedical tools such as hypodermic needles due to their relevance and similarity to cylindrical puncture [27]. However, natural biological puncture systems commonly adopt a tapered, conical tool that reduces to a sharp tip (radius of curvature: $r \sim 100$ μm) [2,7] and often operate within a spectrum of dynamic loading rates ($v \sim$ 1–100 m/s) [50] corresponding to a range of strain rates orders of magnitude higher than a typical quasi-static loading rate ($\dot{\epsilon} \lesssim 0.01$ 1/s). Consequently, predictions from the established models for quasi-static puncture with cylindrical tools might be inadequate to describe the damage morphology and failure behaviors in dynamic, bio-relevant puncture scenarios with sharp conical tools. Moreover, practical challenges may arise when characterizing the failure response of soft materials and tissues at high strain rates using conventional mechanical testing methods such as tensile and tearing tests [51,52], which are designed primarily for relatively low-rate conditions. To address these issues, it is necessary to establish a quantitative relationship between the measurable postmortem characteristics of the dynamic puncture fracture and the ultimate rates-dependent properties to enable experimental-data-based, theory-driven direct failure characterization and biomechanical analysis. Particularly, we introduce a time-dependent constitutive model incorporating both large-deformation nonlinearity and viscoelastic effect to elucidate the rate-based variations in the puncture morphology within a dynamic spectrum.

In this work, we address the above-mentioned gaps in knowledge through systematic characterization of the morphology of the puncture fracture surfaces produced by conical tools in soft materials and tissues. An experimental framework recently proposed by the authors [7] is adapted to achieve highly controllable dynamic conical puncture tests across a wide spectrum of bio-relevant tool geometries (cusp angle: 30°–60°) and dynamic rates ($v \sim$ 9–50 m/s). Systematic quantification reveals that the tangent of the half cusp angle of the undeformed fracture scales with that of the puncture tool, which leads to a rate-based constant angular ratio. This motivates us to construct a theoretical framework within which a quantitative relationship between the constant angular ratio and the target material's rate-dependent extensibility is established. Incorporating the elastic expansion of the puncture cavity, a visco-hyperelastic constitutive model, and a strain–energy–density-based failure criterion, the theoretical framework leads to the postulation of the critical condition of failure in a material exhibiting a 'ductile' fracture response. Predictions for the tensile stretch at failure across a wide spectrum of strain rates find a close agreement with the experimental stretchability results determined independently from the measured angular ratios, validating both the theory and the effectiveness of the puncture method. Leveraging these findings, we aim to elucidate the mechanics of dynamic conical puncture in complex soft material systems and provide the experimental and theoretical bases for the standardization and generalization of the puncture technique as a new method for probing ultimate properties via postmortem failure characterization. To this end, we demonstrate potential applications of the proposed dynamic puncture method in bio-relevant soft materials via two case studies in an ultra-soft and adhesive silicone material and a porcine muscle tissue sample, respectively.

## 2. Materials and methods

### 2.1. Sample preparation

The model silicone elastomer (Solaris, Smooth-On, Inc.) was fabricated following documented procedures [7,53,54] by mixing part A and part B pre-polymer chains as received in a 1:1 ratio (w:w), followed by degassing (≈ 30 min), molding (standard cube mold, ASTM C-109), and curing at room temperature for approximately 1 day. Polycarbonate sheets with 0.02-inch thickness were applied to the inner walls of the mold to improve the transparency of the sample. Sample cubes were examined for dimensions (≈ 49 mm × 49 mm × 42 mm, $t \times w \times h$) and weight (≈ 100 ± 1 g) before being tested.

The low-modulus silicone sample was prepared from a commercial polydimethylsiloxane (PDMS) composite kit as received by mixing the pre-polymer base with the curing agent at a ratio of 55:1 (w:w). Approximately 95 g of liquid mixer was then degassed and molded with a customized cubic polycarbonate mold (≈ 50 mm × 50 mm × 50 mm). After a curing time of approximately 2 days, another 5 g of silicone liquid mixer (Solaris, 4:1 mixing ratio (part A: part B)) was prepared and spread evenly on top of the 55:1 Sylgard sample to create a stiff skin layer after curing for another day. The skin layer seals and protects the subcutaneous material from contamination due to adhesion. The final sample was tested as prepared with the skin side facing the direction of puncture.

A cubic porcine muscle tissue sample (Fig. A6(a), Appendix B) (weight: ≈ 100 g) was cut from a fresh pork loin purchased from a

local grocery store (Meijer, Champaign, IL) using a sharp fillet knife and tested within a time window of one hour. Fat tissues were removed from the test surface. Following the dynamic puncture testing (Sections 2.2 and 5.3), the sample was placed in a freezer for two hours until it became a solid block. A vertical cross-sectional cut was then made along the fracture plane (*i.e.*, the vertical plane passing through the long axis of the crack opening) by pressing a razorblade to split and expose the fracture surface, during which process the damage pattern remains fixed and unmodified (Fig. A6(c): top view; Fig. 6: side view).

### 2.2. Dynamic puncture method

Dynamic conical puncture tests were performed using a customized compressed air cannon (Figs. 1(a), (b) and (c)) (Ballistic Loading and Structural Testing Lab (BLAST), NC State University). 3D printed projectiles (Form 3 stereolithography (SLA) 3D printer, Formlabs Inc., clear resin, FLGPCL04) were selected as puncture tools. Each projectile has a cylindrical base that tapers at a pre-designed cusp angle ($2\theta_{\text{tool}} = [30°, 40°, 50°, 60°]$) to a controlled tip radius ($r \approx 110 \pm 12$ μm). During a puncture test, a projectile is accelerated by the air cannon to a controlled muzzle velocity ($v = [9.4 \pm 0.2$ m/s, $16.1 \pm 0.3$ m/s, $35.1 \pm 0.7$ m/s, $50.3 \pm 1.2$ m/s]) immediately before impacting and penetrating a material sample. A special projectile with a longer cylindrical base was used for the highest puncture speed ($v = 50.3 \pm 1.2$ m/s) to accommodate a large puncture depth that exceeded the available length of the conical region of the projectile. The speed of the projectile at the onset of impact was calculated and calibrated through linear regression of the time vs. displacement data extracted from high-speed imaging (FASTCAM SA-Z, Photron Inc., 10000–30000 fps).

### 2.3. Quasi-static puncture method

Quasi-static puncture tests were performed using a universal test stand (Instron 5944, Instron Inc.) by inserting a conical projectile into a material sample at a controlled feeding speed (10 mm/min). A designed total energy investment ($0.26 \pm 0.01$ J) was applied across the selected cusp angles ($2\theta_{\text{tool}} = [30°, 40°, 50°, 60°]$) by controlling the maximum displacement and the area under the corresponding force–displacement curve. Particularly, the magnitude of the maximum displacement was tuned such that penetration would occur for all tested projectiles (except for the one with $2\theta_{\text{tool}} = 60°$) without exceeding the available length of the conical region.

### 2.4. Characterization of fracture surface

The angular parameters of puncture damage were determined from the resultant triangular planar fracture surfaces in the undeformed configuration. Although the crack produced by puncture may partly close after the removal of the puncture tool, no material healing occurs and the undeformed planar fracture surfaces exhibit good visibility (*e.g.*, Figs. 1(d) and A1). This allowed us to evaluate the crack geometries in two different ways: For a puncture test with a low-to-moderately-high speed ($v \leq 35.1 \pm 0.7$ m/s), identification of the edge lines of the produced fracture surface verifies that a good approximation of its cusp angle ($\theta_{\text{frac}}$) can be obtained from measured dimensions using the relation

$$\tan\theta_{\text{frac}} = \frac{R_{\max}}{D_{\max}}, \tag{1}$$

where $R_{\max}$ is the maximum radial size (*i.e.*, the distance from the centerline to the edge) of the fracture surface, and $D_{\max}$ is the maximum depth of puncture/length of fracture measured from the undeformed triangular fracture surface along the centerline. We determined both $R_{\max}$ and $D_{\max}$ by averaging measurements from microscopic imaging (stereo microscope, M205C, Leica Microsystems Inc.) and manual probing.

For a fracture surface produced at the highest puncture speed ($v = 50.3 \pm 1.2$ m/s), due to a large depth of puncture and rate-induced perturbations of near-surface fracture morphology (as elaborated in Section A3, Appendix B), $\tan\theta_{\text{frac}}$ was evaluated directly in the near-tip region of an undeformed fracture surface using the following equation

$$\tan\theta_{\text{frac}} = \frac{\tan\theta_{\text{proj}}}{\cos\alpha}, \tag{2}$$

where $\theta_{\text{proj}}$ is the projected half cusp angle measured from the microscopic image by identifying the edge lines near the crack tip, and $\alpha$ is the angle between the fracture plane and the focal plane of the microscope (or the horizontal plane in this case). Further information regarding the fracture orientation can be found in Section A1, Appendix B.

## 3. Results

### 3.1. Scaling between fracture and tool cusp angles

In Fig. 2(a), we plot in a log–log scale the tangent values of measured half cusp angles of undeformed fracture surfaces, $\tan\theta_{\text{frac}}$, as a function of the tangent value of the half cusp angle of the corresponding puncture tool, $\tan\theta_{\text{tool}}$, at each of the five applied puncture rate conditions ($v = [9.4 \pm 0.2$ m/s, $16.1 \pm 0.3$ m/s, $35.1 \pm 0.7$ m/s, $50.3 \pm 1.2$ m/s]). In all cases, the magnitude of $\theta_{\text{frac}}$ increases monotonically with increasing $\theta_{\text{tool}}$. Comparing with an identity line (Fig. 2(a), dotted line) reveals that the dependence of $\theta_{\text{frac}}$ on $\theta_{\text{tool}}$ at a prescribed puncture rate can be captured by a simple linear scaling relationship within our selected range of angles

$$\tan\theta_{\text{frac}} = k_A \tan\theta_{\text{tool}}, \tag{3}$$

where $k_A$ is a prefactor. The magnitude of $k_A$ appears to be rate-dependent. For the same applied $\theta_{\text{tool}}$, a fracture surface exhibits a larger $\theta_{\text{frac}}$ value at a higher puncture rate except for the quasi-static condition. In the next section, we show statistically that the ratio between the tangent values of the two angular parameters is indeed a rate-based constant.

### 3.2. Identification of a constant angular ratio

Fig. 2(b) depicts the relationship between $\tan\theta_{\text{frac}}/\tan\theta_{\text{tool}}$ and $\tan\theta_{\text{tool}}$ using the data from Fig. 2(a). The colored dashed lines represent the best results for $k_A$ obtained by fitting Eq. (3) to the angular data in Fig. 2(a) at each applied puncture rate. The resultant $k_A$ and the corresponding $R^2$ values are listed in Table 1. It is evident from Fig. 2(b) and the close-to-one $R^2$ values that the angular ratio, $\tan\theta_{\text{frac}}/\tan\theta_{\text{tool}}$, is approximately a constant independent of variations in $\tan\theta_{\text{tool}}$ at a prescribed puncture rate. Further statistical analysis of the data within the dynamic range using one-way ANOVA confirms that the magnitude of the angular ratio (Fig. 2(b)) statistically differs between the applied puncture rates ($p < 0.001$), and a higher $k_A$ values occurs at a higher rate.

Nevertheless, it appears the rate dependence of the angular ratio is limited within a dynamic range, as the quasi-static results significantly deviate from the dynamic ones ($p < 0.001$), exhibiting the highest $k_A$ value ($k_A \approx 0.899$). However, the angular ratios calculated from quasi-static puncture tests are only nominal values based on the maximum dimensions (Eq. (1)) and might not accurately reflect the relative magnitude of the cusp angle due to the alteration of fracture morphology. In Sections 5.4 and A11 (Appendix B), we discuss the limitations of the angular ratio evaluation arising from the fundamental difference between the fracture mechanics of dynamic and quasi-static conical puncture. Moreover, we include in Figs. 2(a) and (b) a theoretical limit corresponding to the minimum angular ratio ($k_{A,0}$, solid lines) derived from measured material properties and a rate-independent hyperelastic constitutive model (Eq. (10)). A detailed derivation of $k_{A,0}$ as well as further discussion is provided in Section 4.2. Here we note that the calculated angular ratio approaches the theoretical limit as the puncture rate decreases within the dynamic range.

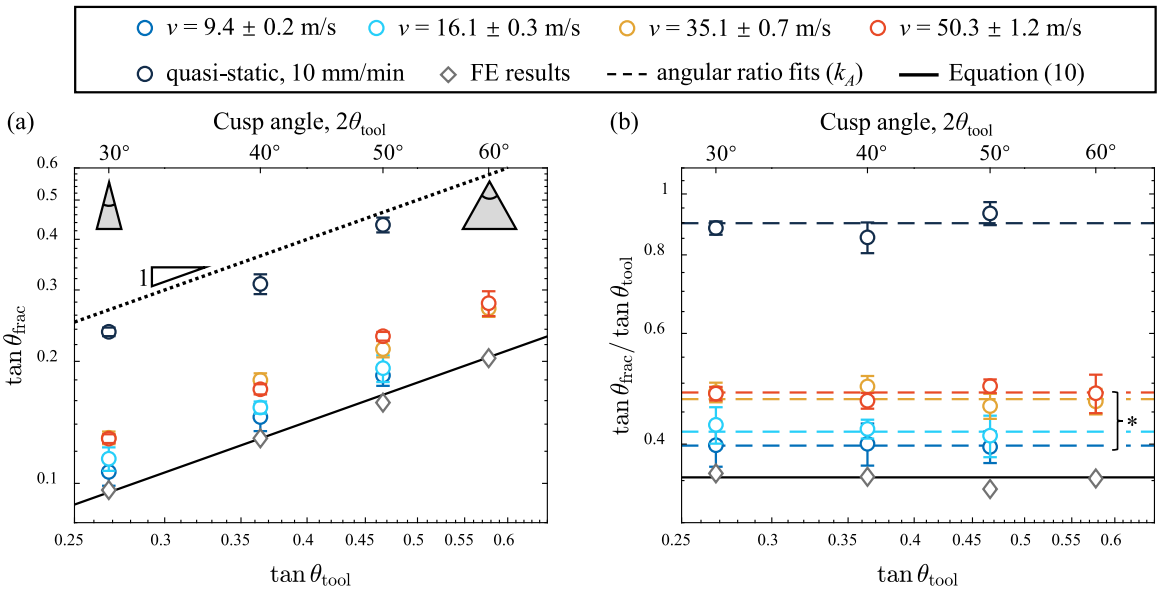


**Fig. 2.** Dependence of angular parameters on rate and tool geometries for both dynamic and quasi-static puncture. (a) $\tan\theta_{frac}$ versus $\tan\theta_{tool}$ results obtained at different puncture rates ($v$ = [9.4 ± 0.2 m/s, 16.1 ± 0.3 m/s, 35.1 ± 0.7 m/s, 50.3 ± 1.2 m/s]) and tool geometries ($2\theta_{tool}$ = [30°, 40°, 50°, 60°]) plotted on a log–log scale. (b) A log–log plot identifying rate-based constant angular ratios, $\tan\theta_{frac}/\tan\theta_{tool}$. The dashed lines indicate the best-fit results ($k_A$) from (a) using Eq. (3). Significant differences ($p < 0.001$) between the dynamic data are marked by *. A black dotted line of a slope of 1 is included in (a) as the upper bound of the 'ductile' puncture response ($\tan\theta_{frac}/\tan\theta_{tool} < 1$). The results in both (a) and (b) are compared with the theoretical rate-independent limit (Eq. (10), black solid lines) and finite element (FE) results obtained from Ref. [7]. Normalized root mean square error (NRMSE) between the theoretical limit and the FE results: NRMSE ≈ 2%.

**Table 1**
Resultant angular ratios and ultimate properties at different puncture rates*.

| $v$ [m/s] | $1.67\times10^{-4}$** | 9.4 ± 0.2 | 16.1 ± 0.3 | 35.1 ± 0.7 | 50.3 ± 1.2 | Theoretical limit |
|---|---|---|---|---|---|---|
| $\dot{\epsilon}$ [1/s] | 0.02 | 1175 ± 25 | 2013 ± 38 | 4388 ± 88 | 6288 ± 150 | – |
| $k_A$ | 0.899 | 0.398 | 0.419 | 0.472 | 0.483 | 0.354 |
| $R^2(k_A)$ | 0.974 | 0.999 | 0.994 | 0.989 | 0.996 | – |
| $\lambda_\theta^*$(experimental) | 1.11 | 2.51 | 2.39 | 2.12 | 2.07 | 2.82 |
| $\lambda_1^*$(experimental) | 1.13 | 2.59 | 2.46 | 2.19 | 2.14 | 2.90 |
| $\lambda_1^*$(theoretical) | 2.90 | 2.55 | 2.44 | 2.25 | 2.18 | 2.90 |

* The errors correspond to standard deviations.

** The quasi-static experimental results represent nominal values.

## 4. Theory

In this section, we explore the material basis of the unique fracture pattern occurring in a dynamic conical puncture scenario. It is evident from Figs. 2(a) and (b) that at a prescribed puncture rate, the damage-tool angular ratio ($\tan\theta_{frac}/\tan\theta_{tool} \sim k_A$) is a rate-dependent material constant. The magnitude of $\tan\theta_{frac}/\tan\theta_{tool}$ approaches a limiting value (*i.e.*, $k_{A,0}$) when the rate decreases within the dynamic range. Here we propose a physical description of the critical deformation state at the onset of puncture crack growth. This, combined with a nonlinear visco-hyperelastic constitutive model incorporating a strain–energy–density-based failure criterion, establishes a theoretical framework that links the experimentally observed constant angular ratios with the rate-dependent elastic stretchability of the model soft elastomeric material via measurable mechanical and failure properties. Ultimately, we aim to lay the groundwork, through generalization, for utilizing the puncture technique as a characterization method to better understand the mechanics and failure of soft biomaterials and biological tissues under dynamic/impact loading.

### 4.1. Puncture cavity expansion

As a starting point, we assume an ideal dynamic puncture scenario in which a conical tool with cusp angle $2\theta_{tool}$ and an extremely sharp tip penetrates a hyperelastic homogeneous half-space composed of a soft, highly deformable material with negligible rate-dependent effect. Although the effective sharpness of a real conical puncture tool depends on both its cusp angle and finite radius of curvature at the tip [2,9,55,56], we note that the puncture tools used in this work have on average a small tip radius of curvature ($r \sim 100$ μm) that is two orders of magnitude smaller than the length scale of the conical puncture region (~ 10 mm). Therefore, we assume that such a sharp tip has a negligible effect on the resultant puncture damage compared to the effect of the cusp angle, as validated by previous dynamic conical puncture experiments by authors [9]. In this case, based on previous [7] and current observations of the puncture damage morphology (Fig. 1(d), Fig. A1, and Section A2 (Appendix B), we assume that a 'ductile' failure response prevails in our selected model material (1:1 Solaris) within a dynamic range. Consequently, the deformed fracture surface conforms to the puncture tool shape; and the undeformed configuration exhibits a smaller planar triangular shape and satisfies $\tan\theta_{frac}/\tan\theta_{tool} < 1$, as shown in Figs. 1(d) and 2, respectively.

To show the connection between the angular parameters and crack growth, we first consider the elastic expansion of a puncture fracture surface (Fig. 3) from the undeformed configuration (Fig. 3(a), orange solid line) to a fully deformed configuration (orange dashed line) perfectly matching the tool shape. Unless otherwise specified, here we use the term 'radial size' to consistently describe either the lateral size ($R(y)$) of an undeformed planar crack or the radius of a conical cavity during the expansion process at an arbitrary depth $y$ from the top surface (Fig. 3). Following the previously established puncture theory [7], we assume that the initial undeformed triangular

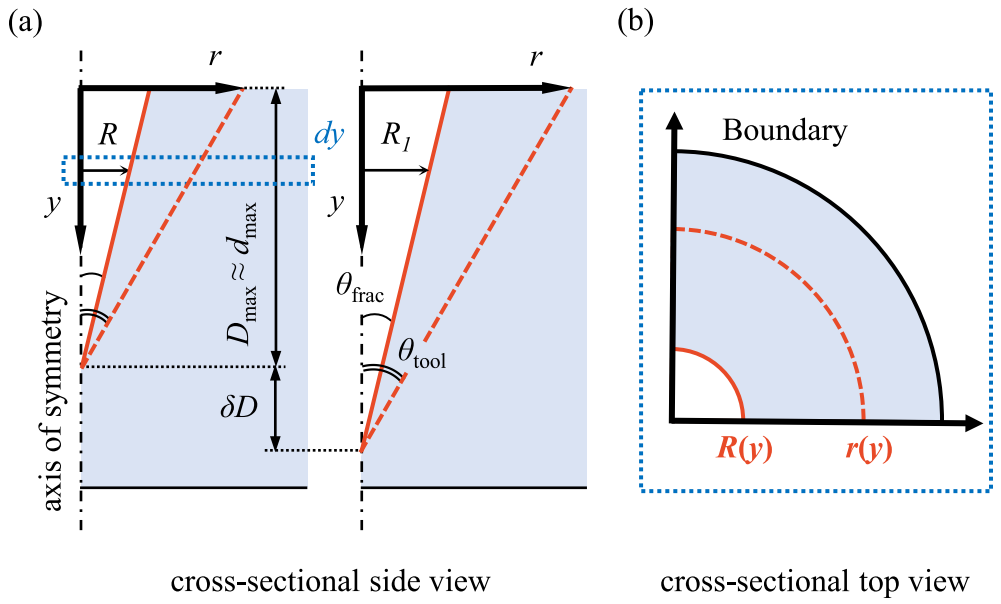


**Fig. 3.** Illustration of the theoretical elastic expansion of puncture cavity. (a) Left: The cavity expands elastically from the initial configuration (orange solid line) to the final deformed configuration conforming to the tool shape (orange dashed line) ($D_{\max} \approx d_{\max}$). Right: For any arbitrary finite growth of depth of puncture, $\delta D$, the radial size of the crack at a coordinate $y$ grows from $R$ to $R_1$ to maintain the geometric similarity. (b) Cross-sectional top view of an infinitesimal slice $dy$ at $y$. Within $dy$, The radial elastic expansion of the opened cavity with a radius $R(y)$ can be approximated by the axisymmetric expansion of a plain-strain cylindrical hole.

planar crack is energetically equivalent to a conical cavity having the same radial size $R(y)$ and cusp angle $2\theta_{\text{frac}}$. The final deformed conical cavity is described by a larger radial size $r(y)$ and cusp angle $2\theta_{\text{tool}}$ corresponding to the puncture tool geometries. As shown in Fig. 3, within an infinitesimal slice, $dy$, at coordinate $y$, the radial expansion of the cavity can be approximated by the axisymmetric growth of a plain-strain circular hole in a cylindrical space (Fig. 3(b)). Therefore, the deformation state at an arbitrary point on the fully deformed cavity wall can be described by the principal stretch components, $(\lambda_r, \lambda_\theta, 1)$, where the radial stretch, $\lambda_r$, and the hoop/circumferential stretch, $\lambda_\theta$, satisfy $\lambda_r = \lambda_\theta^{-1}$ under incompressibility [7]. $\lambda_\theta$ can be estimated using the expression

$$\lambda_\theta \approx \frac{r(y)}{R(y)}, \tag{4}$$

The conical geometries in Fig. 3 give

$$\tan\theta_{\text{frac}} = \frac{R(y)}{D_{max} - y}, \tag{5}$$

and

$$\tan\theta_{\text{tool}} = \frac{r(y)}{d_{max} - y}, \tag{6}$$

where $D_{max}$ and $d_{max}$ are the depths of the initial and deformed cavities, respectively. For simplicity, we assume that the boundary effect associated with elastic indentation has a minor influence on the contact depth. Namely, the undeformed and the deformed cavities largely overlap, and $D_{\max} \approx d_{\max}$ (Fig. 3(a)). Such an assumption has been validated via FE simulations [7]. Substituting Eqs. (5) and (6) into Eq. (4) yields

$$\frac{\tan\theta_{\text{frac}}}{\tan\theta_{\text{tool}}} \approx \frac{1}{\lambda_\theta}. \tag{7}$$

Eq. (7) links the angular ratio to the circumferential deformation on the expanded fracture surface. However, it does not contain information about material failure properties.

### 4.2. Angle regularization in puncture crack growth

Further inspection of the growth of puncture fracture reveals that the deformation state on the wall surface of the fully expanded conical cavity corresponds to the critical conditions at the onset of steady-state crack growth in the radial direction. Such speculation is supported by two particular observations during puncture

1. The radial crack fronts occur on the deformed conical cavity wall, which coincides with the puncture tool surface;
2. The growth of the triangular planar crack surface is self-similar.

The first behavior can be attributed to the high elastic deformability and the associated 'ductile' failure response of the model material (Section A2, Appendix B). Essentially, the steady-state crack propagation is directly driven by the tool-material contact. The second property stems from the continuity of the triangular fracture shape and the invariability of the angular ratio within the same test system. An ensuing implication is that, as illustrated in Fig. 3(a), for any arbitrary finite increase of depth of puncture, $\delta D$, a radial growth of the fracture surface must occur, which satisfies the geometric similarity

$$\left.\frac{R}{R_1}\right|_y \approx \frac{D_{\max} - y}{D_{\max} - y + \delta D}, \tag{8}$$

where $R$ and $R_1$ are the corresponding radial sizes at an arbitrary coordinate of $y$ before and after the growth, respectively. Relating Eq. (8) to Eq. (5) yields

$$\delta R(y) \equiv \left.(R_1 - R)\right|_y = \delta D \tan\theta_{\text{frac}}, \tag{9}$$

where $\delta D$ leads to a finite magnitude of the radial crack growth, $\delta R(y)$. Eq. (9) verifies that the tool-material contact imposes a critical deformation field for crack growth across the entire depth of puncture. Therefore, the crack opening stretch on the deformed fracture cavity, *i.e.*, the hoop stretch $\lambda_\theta$ is theoretically at its ultimate limit, $\lambda_\theta^*$. Consequently, following from Eq. (7), the angular ratio corresponds to the inverse of the material's hoop stretch at failure, *i.e.*,

$$\frac{\tan\theta_{\text{frac}}}{\tan\theta_{\text{tool}}} \approx \frac{1}{\lambda_\theta^*}. \tag{10}$$

To estimate the magnitude of $\lambda_\theta^*$ for our model material (1:1 Solaris) in the rate-independent limit, we assume that the onset of failure occurs at a critical strain–energy–density, $w^*$ [53,54,57]. We approximate $w^*$ by combining a hyperelastic constitutive model and experimentally determined uniaxial tensile extensibility. The constitutive response of 1:1

Solaris silicone elastomer can be well described by the incompressible Arruda-Boyce model [53,54], where the strain–energy–density function takes an approximated form using a five-term series expansion of the inverse Langevin function [58]

$$w = \mu_0 \sum_{i=1}^{5} \frac{C_i}{\lambda_m^{2i-2}} \left(I_1^i - 3^i\right), \tag{11}$$

where $C_1 = \frac{1}{2}$, $C_2 = \frac{1}{20}$, $C_3 = \frac{11}{1050}$, $C_4 = \frac{19}{7000}$, and $C_5 = \frac{519}{673750}$, $I_1 = \lambda_1^2 + \lambda_2^2 + \lambda_3^2$ is the first invariant of the left Cauchy–Green deformation tensor, and $\mu_0$ and $\lambda_m$ are material-dependent fitting parameters. At the critical strain–energy–density for failure, Eq. (11) satisfies

$$w^* = w(I_1^*). \tag{12}$$

The critical first invariant, $I_1^*$, can be calculated as

$$I_1^* = \left(\lambda_1^*\right)^2 + \frac{2}{\lambda_1^*} \approx 9.1, \tag{13}$$

under quasi-static uniaxial tension, with the documented tensile stretch at failure, $\lambda_1^* \approx 2.90$ for 1:1 Solaris [53]. In the case of puncture, the critical first invariant for failure on the surface of the fully deformed conical cavity can be written as

$$I_1^* = \left(\lambda_\theta^*\right)^2 + \left(\lambda_\theta^*\right)^{-2} + 1, \tag{14}$$

under incompressibility. Substituting Eqs. (11), (13), and (14) into Eq. (12), we find that the critical strain–energy–density criterion leads to equal $I_1^*$ values between the two deformation states at failure. Therefore, equating and solving Eqs. (13) and (14) gives an estimation, $\lambda_\theta^* \approx 2.82$, in the rate-independent limit. Correspondingly, we can estimate a theoretical minimum value for the angular ratio using Eq. (10), *i.e.*, $\tan\theta_{\text{frac}}/\tan\theta_{\text{tool}} = k_{A,0} \approx 1/\lambda_\theta^* \approx 0.35$. In Figs. 2(a) and (b), we present this theoretical limit in different forms (black solid lines) in comparison with angular data obtained at different rates (circles) as well as FE results (gray diamonds) calculated from puncture damage simulations in the previous work by the authors [7]. The FE model implements a rate-independent hyperelastic constitutive model and a similar failure criterion based on $w^*$. The FE angular ratios collapse on the theoretical limit (NRMSE ≈ 2%), which validates the above-proposed elastic expansion process and critical hoop deformation state governing the crack angle regularization. Further technical details of the FE simulations for puncture can be found in Appendix B (Section A6) and Ref. [7].

### 4.3. Visco-hyperelastic constitutive model

The above theoretical calculations provide a material basis for the constant angular ratio and its fundamental relationship with the radial crack growth. However, the experimental data in Figs. 2(a) and (b) demand a more comprehensive constitutive model incorporating the ultimate properties at failure (*i.e.*, $w^*$ and $\lambda_1^*$) to address the monotonic rate dependence of the angular constant within the dynamic range. Based on Eq. (10) and the critical energy density criterion (Eqs. (12), (13), and (14)), we estimate lower values of $\lambda_\theta^*$ and $\lambda_1^*$ at higher applied puncture rates for our model material (as tabulated in Table 1) from the best fits for the dynamic angular ratios ($k_A$) in Fig. 2(b). Therefore, we hypothesize that the proposed rate-dependent constitutive model should satisfy the following conditions: (1) The stiffness and the magnitude of stress increase monotonically with the applied strain rate; (2) A lower stretch at failure occurs at a higher strain rate. For this reason, in Appendix A, we adapt the established rate-dependent constitutive model for elastomeric materials [51,59–62] and develop a visco-hyperelastic model by integrating the above Arruda-Boyce model with a linear viscoelastic model via superposition.

In Fig. 4(a), theoretical constitutive response curves corresponding to various applied nominal strain rates in puncture at two different orders of magnitude (quasi-static: $\dot{\varepsilon} = 0.02$ 1/s, and dynamic: $\dot{\varepsilon} \sim 1000$ 1/s) are constructed from Eq. (A.6) using the experimentally-determined Prony series constants (Appendix A). In the limit of the lowest strain rate corresponding to quasi-static puncture, the constitutive response coincides with the rate-independent hyperelastic model. Within the dynamic range, however, the predicted constitutive response exhibits a higher stress magnitude and a significant stiffening effect at a higher strain rate due to the viscoelastic contribution. Such strain-rate-based stiffening behavior is commonly observed in silicone-based elastomeric materials, with extensive experimental evidence from mechanical characterization across a wide spectrum of strain rates (~ 0.01–1000 1/s) [51,59,63–65].

### 4.4. A failure criterion for rate-based ultimate stretch

The reduced extensibility at higher strain rates, which theoretically leads to a lower $\lambda_\theta^*$ and higher angular ratio (Eqs. (13), (14), and (10)), necessitates the implementation of an additional failure criterion for the constitutive model (*i.e.*, Eq (A.6)). Following the discussion in Section 4.2 (Eq. (12)), we again assume that the tensile failure occurs at a critical strain–energy–density, $w^* = w(I_1^*)$. Additionally, we hypothesize that $w^*$ is an intrinsic material failure property independent of rate variations. Therefore, the magnitude of $w^*$ can be determined from either the rate-independent hyperelastic strain–energy–density function (Eq. (11)) or the area under the $S_1^{\text{elas}}$-$\lambda$ constitutive curve (*i.e.*, Eq. (A.3), between $\lambda = 0$ and $\lambda = \lambda_1^* = 2.9$). In Section A8 (Appendix B), we provide a theoretical explanation of the rate independence of $w^*$ based on its scaling relationship with the rate-based critical strain energy release rate ($G$) postulated via a dissipative characteristic length scale and linear viscoelasticity.

With $w^*$ obtained from the hyperelastic model and the knowledge of experimentally determined material constants, we can theoretically predict the rate-dependent tensile extensibility, $\lambda_1^*(\dot{\varepsilon})$, at a given finite strain rate, $\dot{\varepsilon}$, by solving the following constitutive equation

$$w^* = \int_1^{\lambda_1^*(\dot{\varepsilon})} \sigma_1^{\text{eng}}(\lambda, \dot{\varepsilon}) d\lambda, \tag{15}$$

where $\sigma_1^{\text{eng}}(\lambda, \dot{\varepsilon})$ is given by (A.6), and the integral represents the area under the constitutive curve. The resultant $\lambda_1^*(\dot{\varepsilon})$ values at each applied puncture rate are listed in Table 1 in comparison with experimental results and visualized in Fig. 4(a) (vertical dotted lines). As anticipated, the strain-rate-based stiffening effect in conjunction with the assumption of equal tensile toughness (*i.e.*, $w^*$) gives rise to a lower $\lambda_1^*(\dot{\varepsilon})$ value at higher applied $\dot{\varepsilon}$. Finally, we construct a theoretical trend for $\lambda_1^*(\dot{\varepsilon})$ in Fig. 4(b) across a wide spectrum of $\dot{\varepsilon}$.

### 4.5. Comparison between the constitutive model and puncture experiments

We include in Fig. 4(b) experimental $\lambda_1^*$ values as a function of applied $\dot{\varepsilon}$, which are estimated from the angular ratio data of dynamic puncture in Fig. 2(b) using Eqs. (10), (13), and (14). The nominal strain rates for dynamic puncture are determined following the approach described in Section A4 (Appendix B). The data points correspond to the best-fit $k_A$ values, with error bars reflecting the standard deviation of the angular ratio variations across different $\theta_{\text{tool}}$ values in Fig. 2(b). The theoretical predictions in Table 1 and Fig. 4(b) find a good agreement ($R^2 \approx 0.95$) with experimentally determined $\lambda_1^*$ values within our tested dynamic range. Particularly, we emphasize that no data fitting is employed in Table 1 or Fig. 2(b) between the theoretical model and the experimental results; and the rheological data used to determine the Prony series constants (Section A7, Appendix B) are independent of the puncture angular data. The close match between the theoretical and experimental $\lambda_1^*$ values offers solid quantitative evidence that the rate-based variations in puncture angular ratio originate from the viscoelasticity-mediated extensibility of soft materials. It validates the effectiveness of both the visco-hyperelastic model and the dynamic puncture testing for estimating rate-dependent ultimate deformation at high strain rates. Overall, despite the simplicity of our viscoelastic model, it seems that the integration of the Maxwell representation of the stress relaxation function with three elements and six Prony series constants (Appendix A) provides the necessary accuracy to approximate the dynamic response of nonlinear hyperelastic soft materials.

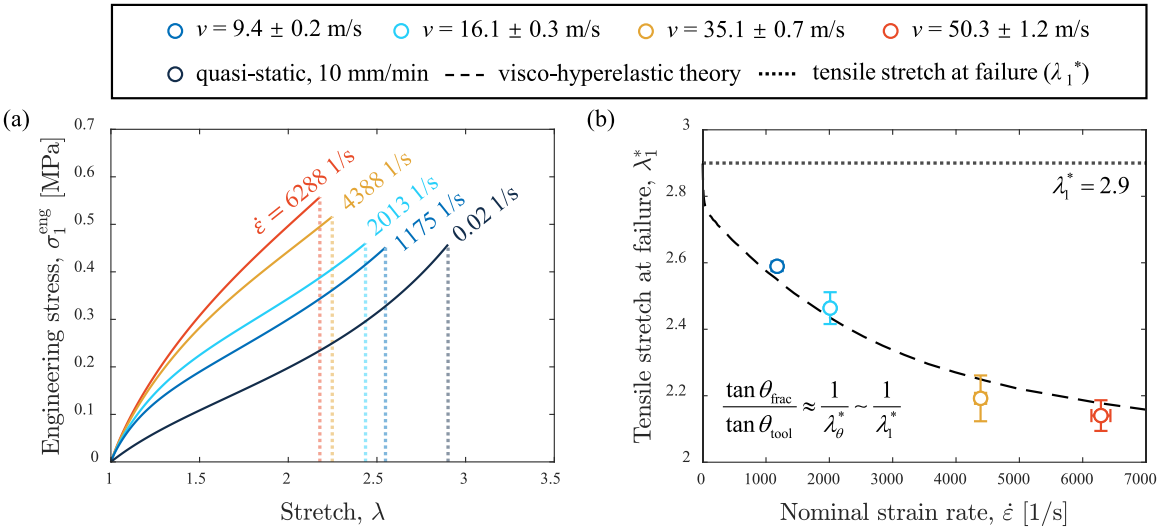


**Fig. 4.** Comparison between the visco-hyperelastic constitutive model and the dynamic puncture experiments for calculated tensile failure response. (a) Theoretical engineering stress ($\sigma_1^{eng}$) versus stretch ($\lambda$) curves predicted by the visco-hyperelastic constitutive model (Eq. (A.6)) at different strain rates corresponding to the puncture rates of interest. The curve corresponding to $\dot{\epsilon} = 0.02$ coincides with the experimental constitutive response obtained via quasi-static uniaxial tensile tests [53]. The vertical dotted lines indicate the estimations for $\lambda_1^*$. (b) The experimental $\lambda_1^*$ versus $\dot{\epsilon}$ results determined from dynamic puncture tests (circles) find a good agreement with the theoretically predicted relationship (dash line) (coefficient of determination: $R^2 \approx 0.95$). The scaling relationships between the angular ratio ($\tan\theta_{frac}/\tan\theta_{tool}$), $\lambda_\theta^*$, and $\lambda_1^*$ are formulated according to Eqs. (10)–(14). The data points correspond to the best-fit $k_A$ values from Fig. 2. Vertical error bars are determined from the standard deviation of the variations in the average $\tan\theta_{frac}/\tan\theta_{tool}$ values in Fig. 2(b). Horizontal error bars correspond to the standard deviation of each selected puncture rate.

## 5. Discussion

### 5.1. Dynamic conical puncture for probing stretchability

The above experimental results in accordance with the visco-hyperelastic constitutive model provide the quantitative basis for the generalization of the dynamic conical puncture method for assessing the stretchability of highly deformable, soft materials. In principle, the puncture technique can serve as an alternative experimental approach to verify and calibrate measurements of stretch at failure obtained via standard mechanical characterization methods such as uniaxial tensile testing. More importantly, it provides a powerful toolbox for the extraction of ultimate properties via postmortem characterization of characteristics of fracture, which is desired in time-sensitive dynamic loading scenarios or at extreme test conditions where conventional mechanical methods might not be feasible — for example, at extremely high strain rates exceeding the operating range of common tensile test devices; in extremely soft and stretchable solids or biomaterials with strong adhesion that are difficult to prepare and manipulate; or in complex biological tissues where it is challenging to obtain test specimens with uniform, controlled geometries. We further demonstrate the capability and potential of dynamic conical puncture in Sections 5.2 and 5.3 via two case studies. In general, to estimate the limiting extensibility of a highly deformable soft material at a given dynamic strain rate, one can potentially carry out dynamic puncture tests according to the following workflow:

1. select a sharp conical puncture tool having a relatively small cusp angle and tip radius (*e.g.*, $2\theta \leq 30°$ and $r \lesssim 100$ μm);
2. use a preliminary dynamic puncture test to calibrate the puncture speed and the elastic indentation depth in the tested material and determine the desired test conditions corresponding to the target nominal strain rate;
3. perform dynamic puncture tests and measure the cusp angle of the resultant undeformed fracture surfaces following Section 2;
4. calculate the average angular ratio and the corresponding hoop stretch at failure using Eqs. (10);
5. estimate the tensile limiting stretch value using the critical strain–energy–density failure criterion (Eqs. (13) and (14)).

### 5.2. A case study for an extremely soft and adhesive elastomer

To further demonstrate the capability of the puncture technique for estimating the extensibility of soft materials having extreme properties, we carry out dynamic puncture tests ($v \sim 10$ m/s) in an ultra-soft and stretchable, commercially available silicone elastomer (Sylgard 184, 55:1 mixing ratio). (Samples preparation follows the procedures introduced in Section 2.1). 55:1 Sylgard is selected because of its unique mechanical characteristics and biomechanical application potential. Silicone-based materials having an extremely low modulus (< 100 KPa) are widely utilized for fundamental research on mechanics of soft material [66–68] and soft biomaterials [19,69–71] for their transparency, high deformability ($\lambda_1^* \gtrsim 3$), strong adhesion, and excellent biocompatibility [72]. In particular, 55:1 Sylgard has a reported elastic modulus of $E \approx 15$ KPa [69], which agrees well with the equilibrium shear modulus of porcine subcutaneous adipose tissue (≈ 5.6 KPa) obtained via rheology [73]. Therefore, 55:1 Sylgard holds the potential as a candidate material to develop a tissue stimulant/phantom for investigating the biological puncture performance in subcutaneous tissues. Nevertheless, the extreme properties of the low-modulus silicone materials can also give rise to various technical complications during sample preparation, handling, and loading due to behaviors such as deformation under self-weight, self-adhesion, folding, and adhesion to untreated surfaces [68,70]. Implementation of traditional mechanical characterization methods is, therefore, challenging and susceptible to uncertainty. Fundamentally, the unique characteristics of low-modulus elastomers stem from a low concentration of the cross-linking agent (< 3% by weight) during fabrication [68], which results in a large number of uncross-linked free polymer chains. Although a special chemical treatment [68] may be used for a silicone sample to extract unreacted polymer molecules and improve its handleability, the process will irreversibly change the mechanical properties of the original material. For the above reasons, an indirect testing mechanism, such as puncture, serves as an adequate alternative approach for estimating the stretch at failure of these low-modulus, ultra-soft materials due to its simple sample preparation and straightforward testing procedures.

In Fig. 5, we show microscopic images of two undeformed fracture surfaces in two 55:1 Sylgard samples produced separately by a puncture tool having cusp angle $2\theta_{tool} = 30°$ and tip radius $r = 40$ μm at a

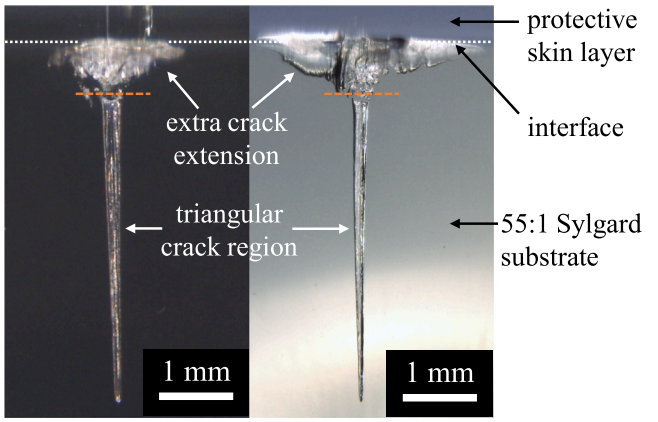


**Fig. 5.** Undeformed fracture surfaces in two 55:1 Sylgard silicone samples. Extra crack extension due to the interfacial effect between the protecting skin layer and the 55:1 Sylgard substrate is visible near the interface, as annotated and separated from the triangular crack region by the orange dashed lines. Puncture rate: $v \approx 10.5$ m/s; Tool geometries: $2\theta_{tool} = 30°$, $r = 40$ μm.

puncture rate of $v \approx 10.5$ m/s. Although the tip of the crack is not visible due to partly closed surfaces, the upper region of the damage (excluding the irregular crack extension caused by the interfacial effect of the protecting skin layer) exhibits a triangular shape and a significantly smaller angle between the two edges compared to that in 1:1 Solaris, indicating a low angular ratio and a large stretch at failure. It allows us to calculate the value of $\tan\theta_{frac}$ using Eq. (2), where the projected half angle $\theta_{proj}$ is measured between the two edge lines. Measurements from two individual puncture tests yield an average angular ratio $\tan\theta_{frac}/\tan\theta_{tool} \approx 9.35 \times 10^{-2}$, which corresponds to average hoop and tensile stretches at failure, $\lambda_\theta^* \approx 10.70$ and $\lambda_1^* \approx 10.74$, respectively. Notably, the calculated $\lambda_1^*$ value is significantly higher (by a factor close to 3) than the interpolated stretchability value for 55:1 Sylgard ($\lambda_1^* \approx 3.8$) using tensile data for low-modulus PDMS materials by Glover et al. [68]. However, such discrepancy is likely contributed by the low defect/flaw tolerance of 55:1 Sylgard under quasi-static loading. A similar flaw-induced significant reduction of stretchability was observed in highly stretchable double-network hydrogels having a similar maximal $\lambda_1^*$ value [74]. Overall, this case study provides experimental evidence for the effectiveness of puncture testing in probing large-deformation failure properties of extremely stretchable and adhesive complex soft polymeric materials.

### 5.3. A case study of puncturing biological tissues

To explore the potential of the puncture method in biomechanics for probing the stretchability of soft biological tissues under dynamic loading, we carried out a case study through a dynamic puncture test in a porcine muscle tissue sample at prescribed test conditions (tool geometries: $2\theta_{tool} = 30°$, $r \approx 104$ μm; puncture rate: $v \approx 10.3$ m/s). Technical details for the sample preparation and images of the sample are provided in Section 2.1 and SI, respectively. An important characteristic of the selected muscle tissue discovered during puncture testing is the absence of a 'brittle' crack extension. This is evident from the post-puncture image (Fig. A6(b), Appendix B) with the puncture tool still embedded inside the tissue sample: No visible gap exists between the contact surfaces of the tool and the damage produced. Such failure behavior implies a high defect/flaw tolerance of the muscle tissue. We speculate that it is potentially contributed by both the hierarchical, fibrous microstructures of muscle as a composite [75,76] and the nonlinear elasticity of passive muscle tissues that incorporates a strong strain-stiffening effect at large deformation [75,77]. A similar high defect tolerance has been previously reported in fibrous collagenous tissues [78], which is associated with a strong crack-blunting effect

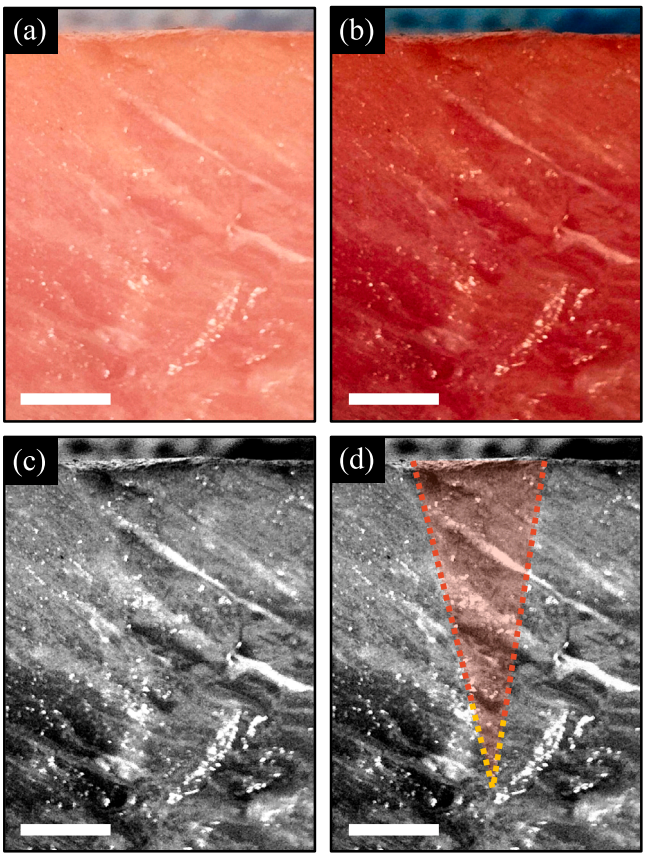


**Fig. 6.** Side-view images of the cross-sectioned porcine muscle tissue sample revealing the triangular puncture damage. (a) Original image. (b) Image with enhanced color saturation. (c) Gray-scale image with enhanced contrast. (d) Dashed guidelines and an orange shaded area identify the crack edge lines and the damaged region, respectively. Extrapolation of the guidelines is indicated by yellow dashed lines. White scale bars: 5 mm.

mediated by microstructures [78]. This unique failure characteristic enables the estimation of the stretchability in the porcine tissue sample using our proposed approach based on either a damage-tool relative size or an angular ratio smaller than one. Fig. 6 shows the post-puncture images of the sample, which was vertically cross-sectioned along the plane of fracture. Despite an anticipated lower stretchability [79] than that of synthetic silicone materials (*e.g.*, 1:1 Solaris), the muscle tissue sample exhibits a puncture morphology corresponding to a more 'ductile' type of failure response. The puncture damage is planar-like and has a penny-shaped opening in the undeformed configuration. It exhibits a triangular shape from the cross-sectional side view (Fig. 6). An estimation of the cusp angle by identifying the edge lines of the damage (Fig. 6(d)) gives an average value, $2\theta_{frac} \approx 22.5° \pm 1°$ (the error indicate the uncertainty of measurement), which corresponds to an angular ratio, $\tan\theta_{frac}/\tan\theta_{tool} \approx 0.74 \pm 0.04$ and stretches at failure, $\lambda_\theta^* \approx 1.35 \pm 0.06$ and $\lambda_1^* \approx 1.39 \pm 0.07$, calculated from the theory established in Section 4. The magnitude of the estimated stretchability falls into a range of reported tensile stretchability values for various mammalian passive muscle tissues ($\lambda_1^* = 1.25$–$1.61$), including rabbit skeletal muscles [79–83], goat skeletal muscles [84], and porcine skeletal muscle fibers [85,86].

The close match between the estimations of the stretch at failure ($\lambda_\theta^*$ and $\lambda_1^*$) for our porcine muscle sample and the documented values support the case study as an initial quantitative verification for the proposed puncture technique in biological tissues. However, it is important to point out that additional considerations regarding the anisotropic behavior and variability of passive muscle tissue need to

be included when utilizing our proposed puncture model to specify its limitations and applicable range, as we discuss in detail in Section A9 (Appendix B).

Broadly, the above case study serves as a proof of concept for future applications of the proposed puncture technique as a new characterization tool for the ultimate properties of biological tissues under dynamic/impact loading. An important scenario of application would be the experimental biomechanics of biological puncture systems. A long-standing challenge in systematic comparative analyses of puncturing organisms varying greatly in scales and functions is the incorporation of a wide spectrum of material properties across both dynamic and static ranges in correlation with conventional mechanical metrics for puncture performance such as the forces and energies required for puncture [2]. With the capability to directly extract ultimate properties associated with large deformation and high strain rates without the assistance of additional mechanical characterization, our proposed method paves the way towards an evidence-based, theory-assisted framework for understanding the biomechanics of puncture. Our future research avenue will focus on the generalization of the puncture method in biological tissues. For example, the currently produced puncture damage has reduced visibility in an opaque tissue sample than in transparent synthetic samples (*e.g.*, Fig. 6(a)) due to the low contrast and similar appearances between the damaged and intact tissues. To address this, a new visualization technique may be introduced to trace the damaged region via, *e.g.*, coloring or powdering.

### 5.4. Limitations in puncture testing: 'ductile' vs. 'brittle' failure

Despite its promising application potential as a characterization tool, the currently proposed experimental framework relies on a key assumption of a 'ductile' failure response. The nearly conformal contact between the tool and crack surfaces necessitates high deformability (comparable or superior to 1:1 Solaris) or a strong crack-blunting effect as a shielding mechanism for flaw growth and crack extension [78]. Otherwise, the apparent fracture morphology can change markedly in a material system exhibiting a 'brittle' failure response. Consequently, a large lateral crack extension exceeding the tool width can significantly complicate the failure characterization. In Section A10 (Appendix B), we further discuss the distinct characteristics between the two types of puncture failure.

Other limitations of the puncture technique likely arise from the rate-mediated transition from a 'ductile' dynamic puncture response to a 'brittle'-like quasi-static response, as observed in our model material (*e.g.*, Fig. 2 and Fig. A1). Compared to the dynamic puncture response, the quasi-static puncture in our model material exhibits not only a unique fracture morphology but also apparent deviations from the theoretical predictions for dynamic conical puncture (Sections 3.2 and A11). This transition of puncture failure behavior implies that the assumption of a 'ductile' failure breaks down as the puncture transitions to a more 'brittle' response at a quasi-static condition. As a result, the predicted relationship between angular ratio and rate-based ultimate stretch values may have a limited applicable range of dynamic strain rates, In Section A11 (Appendix B), we provide further discussion on the morphological differences between quasi-static and dynamic puncture and the possible mechanisms underlying their transition based on the flaw-sensitivity-induced brittleness and reduction of stretchability. Puncture experiments in an expanded range of rates (Fig. A5) provide an estimation for the lower limit of the applicable puncture rates in 1:1 Solaris silicone elastomer ($\sim$ 10 m/s, or $\dot{\epsilon} \sim 1250$ 1/s), below which it is practically challenging to estimate the flaw-insensitive, undiminished stretchability. However, we note that in general the critical condition at the onset of failure-behavioral transition is presumably heavily dependent on the inherent flaw/defect tolerance mediated by microstructures. Therefore, a more flaw-resistant material might exhibit a wider applicable range of rates for probing stretchability via puncture. Future standardization of the puncture technique may focus on the generalization of the criterion for rate-based test conditions across a broader range of soft material systems.

## 6. Concluding remarks

As useful as puncture has been as a mechanical testing technique in exploring the mechanics of biological puncture systems [2,7,8], injury biomechanics [37], and medical tool designs [11,27–30], its potential in characterization of material failure properties is not fully explored. In this work, we demonstrate that at dynamic loading rates, a conical puncture tool produces unique and consistent damage pattern in soft and highly deformable materials. We identify, for the first time, via dynamic conical puncture experiments across a wide spectrum of controlled strain rates and tool geometries that the cusp angles of the damage and tool follow a scaling relationship, and the angular ratio ($\tan\theta_{\text{frac}}/\tan\theta_{\text{tool}}$) is a rate-based material constant. Our theory employing a visco-hyperelastic constitutive model confirms that the magnitude of the angular ratio is related to the rate-dependent hoop and tensile stretches at failure via a strain–energy–density-based failure criterion. Finally, the two case studies demonstrate the capability of the proposed framework and serve as an important initial proof-of-concept towards standardization and future applications of the puncture technique in bio-inspired materials and biological tissues.

Overall, dynamic conical puncture holds the potential of being developed into a standard testing method for probing the rate-dependent ultimate properties of soft solids. However, its current range of application is limited by the type of failure response (Section 5.4), and additional considerations and modifications are necessary for some complex synthetic materials and biological tissues. For example, in swollen hydrogels, poroelasticity may need to be incorporated into the constitutive model to consider the migration of solvent molecules [87]. Such consideration, however, might not be necessary for highly stretchable hydrogels (*e.g.*, double-network (DN) hydrogels) with relatively low or no water content [88] or high-rate dynamic puncture where the local time scale satisfies $t \ll \tau$ and $t \ll l_c^2/D$ (where $\tau$: relaxation time; $l_c$: the characteristic length scale associated with the dissipative process; $D$: diffusivity) [87]. In both cases, the hydrogels behave like a hyperelastic solid. Additionally, the brittleness of some hydrogels may also limit the application of the proposed puncture model, as we point out in Section 5.4. Other examples include biological tissues with pre-existing defects in either macroscale damages/scars caused by trauma or diseases [89], or microstructural imperfections and inhomogeneities. We believe that modification of the proposed puncture model may be necessary, depending on the size, location, and type of the defects, to determine the effect of defect-induced local weaknesses and variations in local properties on the failure process for either diagnostic purposes or isolating the ultimate properties of the tissue matrix. However, such modification might not be required for tissues with small, far-field defects or fibrous materials with strong defect/flaw tolerance [78], where the influence on the homogeneity of the punctured region is limited.

The postmortem damage characterization via dynamic conical puncture approach offers an alternative, time-and-cost-efficient experimental approach for complex material systems having extreme properties, rate-dependent effects, or subjected to dynamic/impact loading with high strain rates ($\dot{\epsilon} \gtrsim 1000$ 1/s). In addition to the damage-tool angular ratio, our proposed experimental framework can also be used for characterizing the depth/length scale of puncture damage [7,9], as a quantitative indicator of the puncture performance. The tradeoffs between the effects of tool sharpness and puncture rate, combined with the findings from this work, can have important implications in engineering and evolutionary biology [7,9]: A dynamic conical puncture system may compensate for suboptimal sharpness by applying a higher puncture rate, which increases the relative size of damage in both the lateral and puncture directions. Moreover, we recognize that our findings from dynamic conical puncture can be generalized to other testing geometries such as sharp-tipped cylindrical puncture tools producing Mode-I 'ductile' fracture (*e.g.*, Ref. [47]). In this case, a cylindrical puncture configuration may be interpreted as a limiting

case of conical puncture where $2\theta_{\text{frac}} \to 0$, and the angular ratio is reduced to a ratio between the radial sizes of the damage and the tool. Ultimately, we hope this work can pave the way for optimized biomedical tool designs and a better understanding of the biomechanics of living puncture systems by offering a theory-assisted experimental framework for characterizing the dynamic failure of biological tissues.

## CRediT authorship contribution statement

**Bingyang Zhang:** Conceptualization, Data curation, Formal analysis, Investigation, Methodology, Validation, Visualization, Writing – original draft, Writing – review & editing. **Philip S.L. Anderson:** Funding acquisition, Methodology, Project administration, Resources, Supervision, Writing – original draft, Writing – review & editing.

## Declaration of competing interest

The authors declare that they have no known competing financial interests or personal relationships that could have appeared to influence the work reported in this paper.

## Data availability

Data will be made available on request.

## Acknowledgments

The authors wish to thank Professor Shelby Hutchens for helpful discussion. This work was supported by the National Science Foundation, United States (grant No. NSF IOS 19-42906 CAR to P. S. L. A.).

## Appendix A. Derivation of the visco-hyperelastic model

In general, a visco-hyperelastic model assumes that the constitutive response of an elastomeric material originates from the superimposition of hyperelasticity and viscoelasticity, which corresponds to low-rate and high-rate responses, respectively. The decoupling of the effects of equilibrium deformation and rate leads to a generalized form for the true stress tensor [62]

$$\boldsymbol{\sigma}(\boldsymbol{\varepsilon}, t) = \boldsymbol{\sigma}^{\mathbf{elas}}(\boldsymbol{\varepsilon}) + \boldsymbol{\sigma}^{\mathbf{vis}}(\boldsymbol{\varepsilon}, t), \tag{A.1}$$

where $\boldsymbol{\sigma}^{\mathbf{elas}}$ is the Cauchy stress tensor, $\boldsymbol{\sigma}^{\mathbf{vis}}$ is the viscoelastic stress tensor, and $\boldsymbol{\varepsilon}$ is the strain tensor. $\boldsymbol{\sigma}$ and $\boldsymbol{\sigma}^{\mathbf{vis}}$ are both functions of the local time scale, $t$. The stress state described by Eq. (A.1) may be visualized using a classic linear viscoelastic spring-dashpot representation as illustrated in Fig. A.7. In this case, the hyperelastic component $\boldsymbol{\sigma}^{\mathbf{elas}}$ is represented by an elastic spring; Three Maxwell spring-dashpot joint elements aligned in parallel correspond to the viscoelastic component $\boldsymbol{\sigma}^{\mathbf{vis}}$.

For an incompressible hyperelastic material, the elastic stress tensor, $\boldsymbol{\sigma}^{\mathbf{elas}}$, takes a general form [7,62]

$$\boldsymbol{\sigma}^{\mathbf{elas}} = -p\mathbf{I} + 2\left[\left(\frac{\partial w}{\partial I_1} + I_1\frac{\partial w}{\partial I_2}\right)\mathbf{B} - \frac{\partial w}{\partial I_2}\mathbf{B}\cdot\mathbf{B}\right], \tag{A.2}$$

where $p$ is an unknown hydrostatic pressure, $\mathbf{I}$ is the identity tensor, $\mathbf{B}$ is the left Cauchy–Green tensor, and $I_2$ is the second invariant of $\mathbf{B}$. Substituting Eq. (11) into Eq. (A.2) and using the loading conditions under uniaxial tension (*i.e.*, $\sigma_2^{\text{elas}} = \sigma_3^{\text{elas}} = 0$, and $\lambda_1 = 1/\lambda_2^2 = 1/\lambda_3^2 = \lambda$), we may calculate the engineering tensile stress, $S_1^{\text{elas}} = \sigma_1^{\text{elas}}/\lambda$, for the Arruda-Boyce model

$$S_1^{\text{elas}}(\lambda) = 2\mu_0\left(\lambda - \frac{1}{\lambda^2}\right)\sum_{i=1}^{5}\frac{iC_i}{\lambda_m^{2i-2}}I_1^{i-1}, \tag{A.3}$$

where the constants $C_1$ to $C_5$ are given in Eq. (11). Here we adopt documented material parameters for 1:1 Solaris silicone elastomer: $\mu_0 \approx 0.08$ MPa and $\lambda_m \approx 2.1$ [7]. They correspond to the best fitting results of the Arruda-Boyce model (Eq. (A.3)) to the experimental stress–stretch data obtained via standard quasi-static uniaxial tensile failure characterization (strain rate: $\sim 0.02$ 1/s) [7].

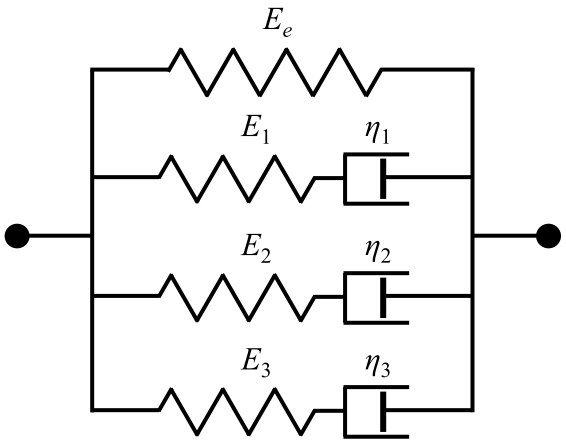


**Fig. A.7.** A spring-dashpot representation of the visco-hyperelastic model with three Maxwell elements. $E_e$ denotes the equilibrium modulus corresponding to the hyperelastic component. The relaxation time for the $i$th Maxwell element is given by $\tau_i = \eta_i/E_i$.

The viscoelastic engineering tensile stress component is approximated using the first three time-dependent terms of the Prony series expansion of the stress relaxation function [51,61,62]

$$S_1^{\text{vis}}(\lambda, t) = \sum_{i=1}^{3}\int_0^t \frac{\partial(S_1^{\text{ins}}(\lambda)g_i)}{\partial\tau}\exp\left(-\frac{t-\tau}{\tau_i}\right)d\tau, \tag{A.4}$$

where $S_1^{\text{ins}}(\lambda)$ denotes the instantaneous tensile stress corresponding to an extremely high rate or a time scale $t = 0$, and $g_i$ and $\tau_i$ are the $i$th Prony series coefficients. Particularly, $\tau_i$ is the relaxation time for the $i$th Maxwell element. The partial derivative in Eq. (A.4) takes the following form in the Maxwell model

$$\frac{\partial(S_1^{\text{ins}}(\lambda)g_i)}{\partial\tau} = E_i\dot{\varepsilon}, \tag{A.5}$$

where $E_i$ is the elastic spring constant of the $i$th Maxwell element, and $\dot{\varepsilon}$ is the nominal strain rate of the system. To estimate the Prony series coefficients, we analyze reported rheological data for 1:1 Solaris by Darby et al. [90] using a Prony series function for storage modulus corresponding to three Maxwell elements [91,92]. Technical details and the results for the data fitting are presented in Section A7 and Fig. A4 (Appendix B). The estimated values for the Prony series constants are $E_1 \approx 0.04$ MPa, $E_2 \approx 0.45$ MPa, $E_3 \approx 0.29$ MPa, $\tau_1 \approx 7.7 \times 10^{-2}$ s, $\tau_2 \approx 1.12 \times 10^{-4}$ s, and $\tau_3 \approx 9.56 \times 10^{-6}$ s. We note that the spring constants agree in order of magnitude with either the elastic constant $\mu_0$ or the elastic modulus of 1:1 Solaris. Particularly, the resultant equilibrium shear modulus calculated from the Prony series fitting, *i.e.*, $G_e \approx 0.13$ MPa (see Section A7, Appendix B) coincides with the experimental shear modulus value of 1:1 Solaris ($\mu = 0.13$ MPa) [7]. To summarize, combining Eqs. (A.3), (A.4), and (A.5), we may rewrite Eq. (A.1) and obtain the engineering visco-hyperelastic constitutive response under tension, *i.e.*

$$\sigma_1^{\text{eng}}(\lambda, \dot{\varepsilon}) = S_1^{\text{elas}}(\lambda) + S_1^{\text{vis}}(\lambda, \dot{\varepsilon}). \tag{A.6}$$

We note that the expanded form of Eq. (A.6) is mathematically equivalent to the classic Fung quasi-linear viscoelastic (QLV) model with a nonlinear separable representation of the relaxation function [61] and number of time-dependent terms, $N = 3$. This approximate form is chosen with considerations of both accuracy and simplicity for describing the nonlinear viscoelastic constitutive response of the model material.

## Appendix B. Supplementary data

Supplementary material related to this article can be found online at https://doi.org/10.1016/j.ijimpeng.2024.104911.

## References


[1] Schofield RMS, Choi S, Coon JJ, Goggans MS, Kreisman TF, Silver DM, et al. Is fracture a bigger problem for smaller animals? Force and fracture scaling for a simple model of cutting, puncture and crushing. Interface Focus 2016;6(3):20160002. http://dx.doi.org/10.1098/rsfs.2016.0002, URL https://royalsocietypublishing.org/doi/10.1098/rsfs.2016.0002.

[2] Anderson PSL. Making a point: shared mechanics underlying the diversity of biological puncture. J Exp Biol 2018;221(22):jeb187294. http://dx.doi.org/10.1242/jeb.187294, http://jeb.biologists.org/lookup/doi/10.1242/jeb.187294, https://journals.biologists.com/jeb/article/221/22/jeb187294/20768/Making-a-point-shared-mechanics-underlying-the.

[3] Crofts SB, Anderson PSL. The influence of cactus spine surface structure on puncture performance and anchoring ability is tuned for ecology. Proc R Soc B: Biol Sci 2018;285(1891):20182280. http://dx.doi.org/10.1098/rspb.2018.2280, URL https://royalsocietypublishing.org/doi/10.1098/rspb.2018.2280.

[4] Crofts SB, Lai Y, Hu Y, Anderson PSL. How do morphological sharpness measures relate to puncture performance in viperid snake fangs? Biol Lett 2019;15(4):20180905. http://dx.doi.org/10.1098/rsbl.2018.0905, URL https://royalsocietypublishing.org/doi/10.1098/rsbl.2018.0905.

[5] Anderson PSL, Crofts SB, Kim J-T, Chamorro LP. Taking a stab at quantifying the energetics of biological puncture. Integr Comp Biol 2019;59(6):1586–96. http://dx.doi.org/10.1093/icb/icz078, URL https://academic.oup.com/icb/article/59/6/1586/5505432.

[6] Galloway KA, Porter ME. Predator–prey interactions examined using lionfish spine puncture performance. Integr Organ Biol 2021;3(1). http://dx.doi.org/10.1093/iob/obaa049, URL https://academic.oup.com/iob/article/doi/10.1093/iob/obaa049/6121261.

[7] Zhang B, Anderson PSL. Modelling biological puncture: a mathematical framework for determining the energetics and scaling. J R Soc Interface 2022;19(195). http://dx.doi.org/10.1098/rsif.2022.0559, URL https://royalsocietypublishing.org/doi/10.1098/rsif.2022.0559.

[8] Anderson PSL, Kawano SM. Different traits at different rates: The effects of dynamic strain rate on structural traits in biology. Integr Comp Biol 2022;62(3):683–99. http://dx.doi.org/10.1093/icb/icac066, URL https://academic.oup.com/icb/article/62/3/683/6595973.

[9] Zhang B, Anderson PSL. Investigation of the rate-mediated form-function relationship in biological puncture. Sci Rep 2023;13(1):12097. http://dx.doi.org/10.1038/s41598-023-39092-8, https://www.nature.com/articles/s41598-023-39092-8.

[10] Ankersen J, Birkbeck AE, Thomson RD, Vanezis P. Puncture resistance and tensile strength of skin simulants. Proc Inst Mech Eng H 1999;213(6):493–501. http://dx.doi.org/10.1243/0954411991535103, URL http://journals.sagepub.com/doi/10.1243/0954411991535103.

[11] Abolhassani N, Patel R, Moallem M. Needle insertion into soft tissue: A survey. Med Eng Phys 2007;29(4):413–31. http://dx.doi.org/10.1016/j.medengphy.2006.07.003.

[12] Mahvash M, Dupont P. Fast needle insertion to minimize tissue deformation and damage. In: 2009 IEEE international conference on robotics and automation. IEEE; 2009, p. 3097–102. http://dx.doi.org/10.1109/ROBOT.2009.5152617, URL http://ieeexplore.ieee.org/document/5152617/.

[13] Zhu D, Szewciw L, Vernerey F, Barthelat F. Puncture resistance of the scaled skin from striped bass: Collective mechanisms and inspiration for new flexible armor designs. J Mech Behav Biomed Mater 2013;24:30–40. http://dx.doi.org/10.1016/j.jmbbm.2013.04.011, https://linkinghub.elsevier.com/retrieve/pii/S1751616113001343.

[14] Wang Y, Tai BL, Yu H, Shih AJ. Silicone-based tissue-mimicking phantom for needle insertion simulation. J Med Dev 2014;8(2):1–7. http://dx.doi.org/10.1115/1.4026508, URL https://asmedigitalcollection.asme.org/medicaldevices/article/doi/10.1115/1.4026508/448103/SiliconeBased-TissueMimicking-Phantom-for-Needle.

[15] Bao X, Li W, Lu M, Zhou Z. Experiment study on puncture force between MIS suture needle and soft tissue. Biosurf Biotribol 2016;2(2):49–58. http://dx.doi.org/10.1016/j.bsbt.2016.05.001, URL https://linkinghub.elsevier.com/retrieve/pii/S2405451816300101.

[16] Aoyagi S, Okuda K, Takahashi T, Suzuki M. Effect of microneedle cross-sectional shape on puncture resistance – investigation of polygonal and star-shaped cross sections. J Robot Mechatron 2020;32(2):371–81. http://dx.doi.org/10.20965/jrm.2020.p0371.

[17] Yan Q, Weng J, Shen S, Wang Y, Fang M, Zheng G, et al. Finite element analysis for biodegradable dissolving microneedle materials on skin puncture and mechanical performance evaluation. Polymers 2021;13(18):3043. http://dx.doi.org/10.3390/polym13183043, URL https://www.mdpi.com/2073-4360/13/18/3043.

[18] Fregonese S, Bacca M. Piercing soft solids: A mechanical theory for needle insertion. J Mech Phys Solids 2021;154(August 2020):104497. http://dx.doi.org/10.1016/j.jmps.2021.104497, https://linkinghub.elsevier.com/retrieve/pii/S0022509621001654.

[19] Maiorana CH, Jotawar RA, German GK. Biomechanical fracture mechanics of composite layered skin-like materials. Soft Matter 2022;18(10):2104–12. http://dx.doi.org/10.1039/D1SM01187A, URL http://xlink.rsc.org/?DOI=D1SM01187A.

[20] dong Bao Y, qian Qu S, bo Qi D, Wei W. Investigation on puncture mechanical performance of tracheal tissue. J Mech Behav Biomed Mater 2022;125(October 2021):104958. http://dx.doi.org/10.1016/j.jmbbm.2021.104958.

[21] Montanari M, Brighenti R, Terzano M, Spagnoli A. Puncturing of soft tissues: experimental and fracture mechanics-based study. Soft Matter 2023;19(20):3629–39. http://dx.doi.org/10.1039/D3SM00011G, https://linkinghub.elsevier.com/retrieve/pii/S1751616121005890, http://xlink.rsc.org/?DOI=D3SM00011G.

[22] Pollock TI, Hocking DP, Evans AR. The killer's toolkit: remarkable adaptations in the canine teeth of mammalian carnivores. Zool J Linnean Soc 2022;196(3):1138–55. http://dx.doi.org/10.1093/zoolinnean/zlab064, https://academic.oup.com/zoolinnean/advance-article/doi/10.1093/zoolinnean/zlab064/6370237, https://academic.oup.com/zoolinnean/article/196/3/1138/6370237.

[23] Emlen DJ. The evolution of animal weapons. Annu Rev Ecol Evol Syst 2008;39:387–413. http://dx.doi.org/10.1146/annurev.ecolsys.39.110707.173502.

[24] Jensen KH, Knoblauch J, Christensen AH, Haaning KS, Park K. Universal elastic mechanism for stinger design. Nat Phys 2020;16(10):1074–8. http://dx.doi.org/10.1038/s41567-020-0930-9, http://www.nature.com/articles/s41567-020-0930-9.

[25] Cerkvenik U, van de Straat B, Gussekloo SWS, van Leeuwen JL. Mechanisms of ovipositor insertion and steering of a parasitic wasp. Proc Natl Acad Sci 2017;114(37):E7822–31. http://dx.doi.org/10.1073/pnas.1706162114, http://www.pnas.org/lookup/doi/10.1073/pnas.1706162114, https://pnas.org/doi/full/10.1073/pnas.1706162114.

[26] Bar-On B. On the form and bio-mechanics of venom-injection elements. Acta Biomater 2019;85:263–71. http://dx.doi.org/10.1016/j.actbio.2018.12.030.

[27] Shergold OA, Fleck NA. Mechanisms of deep penetration of soft solids, with application to the injection and wounding of skin. Proc R Soc Lond Ser A Math Phys Eng Sci 2004;460(2050):3037–58. http://dx.doi.org/10.1098/rspa.2004.1315, URL https://royalsocietypublishing.org/doi/10.1098/rspa.2004.1315.

[28] Han P, Che D, Pallav K, Ehmann K. Models of the cutting edge geometry of medical needles with applications to needle design. Int J Mech Sci 2012;65(1):157–67. http://dx.doi.org/10.1016/j.ijmecsci.2012.09.014, https://linkinghub.elsevier.com/retrieve/pii/S0020740312002184.

[29] Leibinger A, Oldfield MJ, Rodriguez y Baena F. Minimally disruptive needle insertion: a biologically inspired solution. Interface Focus 2016;6(3):20150107. http://dx.doi.org/10.1098/rsfs.2015.0107, URL https://royalsocietypublishing.org/doi/10.1098/rsfs.2015.0107.

[30] Li AD, Putra KB, Chen L, Montgomery JS, Shih A. Mosquito proboscis-inspired needle insertion to reduce tissue deformation and organ displacement. Sci Rep 2020;10(1):1–14. http://dx.doi.org/10.1038/s41598-020-68596-w.

[31] Misra S, Reed KB, Douglas AS, Ramesh KT, Okamura AM. Needle-tissue interaction forces for bevel-tip steerable needles. In: 2008 2nd IEEE RAS & EMBS international conference on biomedical robotics and biomechatronics. IEEE; 2008, p. 224–31. http://dx.doi.org/10.1109/BIOROB.2008.4762872, URL https://ieeexplore.ieee.org/document/4762872/.

[32] Giovannini M, Ren H, Wang X, Ehmann K. Tissue cutting with microserrated biopsy punches. J Micro Nano-Manufact 2017;5(4):1–8. http://dx.doi.org/10.1115/1.4037726.

[33] Fakhouri S, Hutchens SB, Crosby AJ. Puncture mechanics of soft solids. Soft Matter 2015;11(23):4723–30. http://dx.doi.org/10.1039/C5SM00230C, arXiv:barataMaterialsandTechniquesofpolychromewoodensculpture, URL http://xlink.rsc.org/?DOI=C5SM00230C.

[34] Fakhouri S. Cavitation and puncture for mechanical measurement of soft solids (Ph.D. thesis), University of Massachusetts Amherst; 2015, p. 297. http://dx.doi.org/10.7275/6436150.0, URL http://scholarworks.umass.edu/dissertations_2.

[35] Rattan S, Crosby AJ. Effect of polymer volume fraction on fracture initiation in soft gels at small length scales. ACS Macro Lett 2019;8(5):492–8. http://dx.doi.org/10.1021/acsmacrolett.9b00086, URL https://pubs.acs.org/doi/10.1021/acsmacrolett.9b00086.

[36] Boots JN, Brake DW, Clough JM, Tauber J, Ruiz-Franco J, Kodger TE, et al. Quantifying bond rupture during indentation fracture of soft polymer networks using molecular mechanophores. Phys Rev Mater 2022;6(2):1–11. http://dx.doi.org/10.1103/PhysRevMaterials.6.025605.

[37] Bull AMJ, Clasper J, Mahoney PF, editors. Blast injury science and engineering. vol. 1, Cham: Springer International Publishing; 2016, p. 321. http://dx.doi.org/10.1007/978-3-319-21867-0, URL http://link.springer.com/10.1007/978-3-319-21867-0.

[38] Stevenson A, Malek KA. On the puncture mechanics of rubber. Rubber Chem Technol 1994;67(5):743–60. http://dx.doi.org/10.5254/1.3538707, URL https://meridian.allenpress.com/rct/article/67/5/743/92122/On-the-Puncture-Mechanics-of-Rubber.

[39] Oldfield M, Dini D, Giordano G, Rodriguez y Baena F. Detailed finite element modelling of deep needle insertions into a soft tissue phantom using a cohesive approach. Comput Methods Biomech Biomed Eng 2013;16(5):530–43. http://dx.doi.org/10.1080/10255842.2011.628448, URL http://www.tandfonline.com/doi/abs/10.1080/10255842.2011.628448.

[40] Kundanati L, Guarino R, Menegon M, Pugno NM. Mechanics of snake biting: Experiments and modelling. J Mech Behav Biomed Mater 2020;112(July):104020. http://dx.doi.org/10.1016/j.jmbbm.2020.104020, https://linkinghub.elsevier.com/retrieve/pii/S1751616120305713.

[41] Fregonese S, Bacca M. How friction and adhesion affect the mechanics of deep penetration in soft solids. Soft Matter 2022;18(36):6882–7. http://dx.doi.org/10.1039/D2SM00638C, URL http://xlink.rsc.org/?DOI=D2SM00638C.

[42] Fregonese S, Tong Z, Wang S, Bacca M. Theoretical puncture mechanics of soft compressible solids. J Appl Mech 2023;90(11):1–7. http://dx.doi.org/10.1115/1.4062844, URL https://asmedigitalcollection.asme.org/appliedmechanics/article/90/11/111003/1164197/Theoretical-Puncture-Mechanics-of-Soft.

[43] Spagnoli A, Brighenti R, Alberini R, Montanari M, Terzano M. On Mode i crack mechanism in the puncturing of soft tissues. Proc Struct Integr 2022;41(C):656–63. http://dx.doi.org/10.1016/j.prostr.2022.05.074.

[44] Jussila J. Measurement of kinetic energy dissipation with gelatine fissure formation with special reference to gelatine validation. Forensic Sci Int 2005;150(1):53–62. http://dx.doi.org/10.1016/j.forsciint.2004.06.038, URL https://linkinghub.elsevier.com/retrieve/pii/S0379073804004116.

[45] Coupland RM, Rothschild MA, Thali MJ. Wound ballistics. Berlin, Heidelberg: Springer Berlin Heidelberg; 2011, http://dx.doi.org/10.1007/978-3-642-20356-5, URL http://link.springer.com/10.1007/978-3-642-20356-5.

[46] Milner MP, Hutchens SB. Dynamic fracture of expanding cavities in nonlinear soft solids. J Appl Mech 2021;88(8). http://dx.doi.org/10.1115/1.4051431, URL https://asmedigitalcollection.asme.org/appliedmechanics/article/88/8/081008/1110838/Dynamic-Fracture-of-Expanding-Cavities-in.

[47] Shergold OA, Fleck NA. Experimental investigation into the deep penetration of soft solids by sharp and blunt punches, with application to the piercing of skin. J Biomech Eng 2005;127(5):838–48. http://dx.doi.org/10.1115/1.1992528.

[48] van Gerwen DJ, Dankelman J, van den Dobbelsteen JJ. Needle–tissue interaction forces – A survey of experimental data. Med Eng Phys 2012;34(6):665–80. http://dx.doi.org/10.1016/j.medengphy.2012.04.007, https://linkinghub.elsevier.com/retrieve/pii/S1350453312000938.

[49] Mohammadi H, Ebrahimian A, Maftoon N. Fracture behaviour of human skin in deep needle insertion can be captured using validated cohesive zone finite-element method. Comput Biol Med 2021;139(July):104982. http://dx.doi.org/10.1016/j.compbiomed.2021.104982, https://linkinghub.elsevier.com/retrieve/pii/S0010482521007769.

[50] Anderson PSL, LaCosse J, Pankow M. Point of impact: the effect of size and speed on puncture mechanics. Interface Focus 2016;6(3):20150111. http://dx.doi.org/10.1098/rsfs.2015.0111, URL https://royalsocietypublishing.org/doi/10.1098/rsfs.2015.0111.

[51] Guo L, Lv Y, Deng Z, Wang Y, Zan X. Tension testing of silicone rubber at high strain rates. Polym Test 2016;50:270–5. http://dx.doi.org/10.1016/j.polymertesting.2016.01.021, https://linkinghub.elsevier.com/retrieve/pii/S0142941815303093.

[52] Mai T-T, Okuno K, Tsunoda K, Urayama K. Crack-tip strain field in supershear crack of elastomers. ACS Macro Lett 2020;9(5):762–8. http://dx.doi.org/10.1021/acsmacrolett.0c00213, URL https://pubs.acs.org/doi/10.1021/acsmacrolett.0c00213.

[53] Zhang B, Hutchens SB. On the relationship between cutting and tearing in soft elastic solids. Soft Matter 2021;17(28):6728–41. http://dx.doi.org/10.1039/D1SM00527H, URL http://xlink.rsc.org/?DOI=D1SM00527H.

[54] Zhang B. Y-shaped cutting as a characterization method for the failure of soft elastic solids (Ph.D. thesis), University of Illinois Urbana-Champaign; 2021, URL https://hdl.handle.net/2142/113945.

[55] Freeman PW, Lemen CA. The trade-off between tooth strength and tooth penetration: predicting optimal shape of canine teeth. J Zool 2007;273(3):273–80. http://dx.doi.org/10.1111/j.1469-7998.2007.00325.x, URL https://onlinelibrary.wiley.com/doi/10.1111/j.1469-7998.2007.00325.x.

[56] Zhang B, Shiang C-S, Yang S, Hutchens S. Y-shaped cutting for the systematic characterization of cutting and tearing. Exp Mech 2019;59(4):517–29. http://dx.doi.org/10.1007/s11340-019-00479-2, URL http://link.springer.com/10.1007/s11340-019-00479-2.

[57] Long R, Hui C-Y, Gong JP, Bouchbinder E. The fracture of highly deformable soft materials: A tale of two length scales. Ann Rev Condens Matter Phys 2021;12(1):71–94. http://dx.doi.org/10.1146/annurev-conmatphys-042020-023937, arXiv:2004.03159.

[58] Boyce MC. Direct comparison of the gent and the arruda-boyce constitutive models of rubber elasticity. Rubber Chem Technol 1996;69(5):781–5. http://dx.doi.org/10.5254/1.3538401, URL https://meridian.allenpress.com/rct/article/69/5/781/92351/Direct-Comparison-of-the-Gent-and-the-ArrudaBoyce.

[59] Shim VPW, Yang LM, Lim CT, Law PH. A visco-hyperelastic constitutive model to characterize both tensile and compressive behavior of rubber. J Appl Polym Sci 2004;92(1):523–31. http://dx.doi.org/10.1002/app.20029, URL https://onlinelibrary.wiley.com/doi/10.1002/app.20029.

[60] Hoo Fatt MS, Ouyang X. The behavior of elastomers at high strain rates. In: Structures under shock and impact IX. WIT transactions on the built environment, Vol 87, 1, Southampton, UK: WIT Press; 2006, p. 97–106. http://dx.doi.org/10.2495/SU060101, URL http://library.witpress.com/viewpaper.asp?pcode=SU06-010-1.

[61] Nekouzadeh A, Genin GM. Adaptive quasi-linear viscoelastic modeling. In: Biomechanics and mechanobiology of aneurysms. Springer, Berlin, Heidelberg; 2012, p. 47–83. http://dx.doi.org/10.1007/8415_2012_142, URL https://link.springer.com/10.1007/8415_2012_142.

[62] Khajehsaeid H, Arghavani J, Naghdabadi R, Sohrabpour S. A visco-hyperelastic constitutive model for rubber-like materials: A rate-dependent relaxation time scheme. Internat J Engrg Sci 2014;79:44–58. http://dx.doi.org/10.1016/j.ijengsci.2014.03.001.

[63] Shergold OA, Fleck NA, Radford D. The uniaxial stress versus strain response of pig skin and silicone rubber at low and high strain rates. Int J Impact Eng 2006;32(9):1384–402. http://dx.doi.org/10.1016/j.ijimpeng.2004.11.010, URL https://linkinghub.elsevier.com/retrieve/pii/S0734743X04002325.

[64] Khanafer K, Duprey A, Schlicht M, Berguer R. Effects of strain rate, mixing ratio, and stress-strain definition on the mechanical behavior of the polydimethylsiloxane (PDMS) material as related to its biological applications. Biomed Microdev 2009;11(2):503–8. http://dx.doi.org/10.1007/s10544-008-9256-6.

[65] Tateyama K, Yamada H, Ogasawara N. Effect of strain rate on compressive behaviour of silicone rubber. In: Buzaud E, Cosculluela A, Couque H, Cadoni E, editors. EPJ Web Conf 2018;183:02044. http://dx.doi.org/10.1051/epjconf/201818302044, URL https://www.epj-conferences.org/10.1051/epjconf/201818302044.

[66] Zhang B. Fabrication and mechanical characterization of liquid-in-solid elastomeric soft composites (Thesis), University of Illinois Urbana-Champaign; 2016, URL http://hdl.handle.net/2142/90842.

[67] Milner MP, Jin L, Hutchens SB. Creasing in evaporation-driven cavity collapse. Soft Matter 2017;13:6894–904. http://dx.doi.org/10.1039/C7SM01258F, URL http://xlink.rsc.org/?DOI=C7SM01258F.

[68] Glover JD, McLaughlin CE, McFarland MK, Pham JT. Extracting uncrosslinked material from low modulus sylgard 184 and the effect on mechanical properties. J Polym Sci 2020;58(2):343–51. http://dx.doi.org/10.1002/pol.20190032.

[69] Cesa CM, Kirchgeßner N, Mayer D, Schwarz US, Hoffmann B, Merkel R. Micropatterned silicone elastomer substrates for high resolution analysis of cellular force patterns. Rev Sci Instrum 2007;78(3). http://dx.doi.org/10.1063/1.2712870.

[70] Chin CD, Khanna K, Sia SK. A microfabricated porous collagen-based scaffold as prototype for skin substitutes. Biomed Microdev 2008;10(3):459–67. http://dx.doi.org/10.1007/s10544-007-9155-2, URL http://link.springer.com/10.1007/s10544-007-9155-2.

[71] Pham JT, Xue L, del Campo A, Salierno M. Guiding cell migration with microscale stiffness patterns and undulated surfaces. Acta Biomater 2016;38:106–15. http://dx.doi.org/10.1016/j.actbio.2016.04.031, https://linkinghub.elsevier.com/retrieve/pii/S1742706116301933.

[72] Miranda I, Souza A, Sousa P, Ribeiro J, Castanheira EMS, Lima R, et al. Properties and applications of PDMS for biomedical engineering: A review. J Funct Biomater 2021;13(1):2. http://dx.doi.org/10.3390/jfb13010002, URL https://www.mdpi.com/2079-4983/13/1/2.

[73] Geerligs M, Peters GW, Ackermans PA, Oomens CW, Baaijens FP. Linear viscoelastic behavior of subcutaneous adipose tissue. Biorheology 2008;45(6):677–88. http://dx.doi.org/10.3233/BIR-2008-0517, URL https://www.medra.org/servlet/aliasResolver?alias=iospress&doi=10.3233/BIR-2008-0517.

[74] Zhou Y, Hu J, Zhao P, Zhang W, Suo Z, Lu T. Flaw-sensitivity of a tough hydrogel under monotonic and cyclic loads. J Mech Phys Solids 2021;153(February):104483. http://dx.doi.org/10.1016/j.jmps.2021.104483, https://linkinghub.elsevier.com/retrieve/pii/S0022509621001526.

[75] Odegard GM, Haut Donahue TL, Morrow DA, Kaufman KR. Constitutive modeling of skeletal muscle tissue with an explicit strain-energy function. J Biomech Eng 2008;130(6):1–9. http://dx.doi.org/10.1115/1.3002766, URL https://asmedigitalcollection.asme.org/biomechanical/article/doi/10.1115/1.3002766/456013/Constitutive-Modeling-of-Skeletal-Muscle-Tissue.

[76] Lieber RL, Binder-Markey BI. Biochemical and structural basis of the passive mechanical properties of whole skeletal muscle. J Physiol 2021;599(16):3809–23. http://dx.doi.org/10.1113/JP280867, URL https://onlinelibrary.wiley.com/doi/10.1113/JP280867.

[77] Herbert R. The passive mechanical properties of muscle and their adaptations to altered patterns of use. Australian J Physiother 1988;34(3):141–9. http://dx.doi.org/10.1016/S0004-9514(14)60606-1, https://linkinghub.elsevier.com/retrieve/pii/S0004951414606061.

[78] Bircher K, Zündel M, Pensalfini M, Ehret AE, Mazza E. Tear resistance of soft collagenous tissues. Nature Commun 2019;10(1):792. http://dx.doi.org/10.1038/s41467-019-08723-y, URL http://www.nature.com/articles/s41467-019-08723-y.

[79] Van Ee CA, Chasse AL, Myers BS. Quantifying skeletal muscle properties in cadaveric test specimens: Effects of mechanical loading, postmortem time, and freezer storage. J Biomech Eng 2000;122(1):9–14. http://dx.doi.org/10.1115/1.429621, URL https://asmedigitalcollection.asme.org/biomechanical/article/122/1/9/447253/Quantifying-Skeletal-Muscle-Properties-in.

[80] Garrett WE, Safran MR, Seaber AV, Glisson RR, Ribbeck BM. Biomechanical comparison of stimulated and nonstimulated skeletal muscle pulled to failure. Am J Sports Med 1987;15(5):448–54. http://dx.doi.org/10.1177/036354658701500504, URL http://journals.sagepub.com/doi/10.1177/036354658701500504.

[81] Best TM. A biomechanical study of skeletal muscle strain injuries (Ph.D. thesis), Duke University; 1993, URL https://www.proquest.com/dissertations-theses/biomechanical-study-skeletal-muscle-strain/docview/304075692/se-2.

[82] Myers BS, Van Ee CA, Camacho DLA, Woolley CT, Best TM. On the structural and material properties of mammalian skeletal muscle and its relevance to human cervical impact dynamics. In: SAE technical papers. 1995, http://dx.doi.org/10.4271/952723, URL https://www.sae.org/content/952723/.

[83] Morrow DA, Haut Donahue TL, Odegard GM, Kaufman KR. Transversely isotropic tensile material properties of skeletal muscle tissue. J Mech Behav Biomed Mater 2010;3(1):124–9. http://dx.doi.org/10.1016/j.jmbbm.2009.03.004, https://linkinghub.elsevier.com/retrieve/pii/S1751616109000472.

[84] Kuthe CD, Uddanwadiker RV. Investigation of effect of fiber orientation on mechanical behavior of skeletal muscle. J Appl Biomater Funct Mater 2016;14(2):e154–62. http://dx.doi.org/10.5301/jabfm.5000275.

[85] Mutungi G, Purslow P, Warkup C. Influence of temperature, fibre diameter and conditioning on the mechanical properties of single muscle fibres extended to fracture. J Sci Food Agric 1996;72(3):359–66. http://dx.doi.org/10.1002/(SICI)1097-0010(199611)72:3<359::AID-JSFA667>3.0.CO;2-H, https://onlinelibrary.wiley.com/doi/10.1002/(SICI)1097-0010(199611)72:3<359::AID-JSFA667>3.0.CO;2-H.

[86] Christensen M, Kok C, Ertbjerg P. Mechanical properties of type I and type IIB single porcine muscle fibres. Meat Sci 2006;73(3):422–5. http://dx.doi.org/10.1016/j.meatsci.2005.12.010, URL https://linkinghub.elsevier.com/retrieve/pii/S0309174006000027.

[87] Hu Y, Suo Z. Viscoelasticity and poroelasticity in elastomeric gels. Acta Mech Solida Sin 2012;25(5):441–58. http://dx.doi.org/10.1016/S0894-9166(12)60039-1, URL http://linkinghub.elsevier.com/retrieve/pii/S0894916612600391.

[88] Chen Q, Chen H, Zhu L, Zheng J. Fundamentals of double network hydrogels. J Mater Chem B 2015;3(18):3654–76. http://dx.doi.org/10.1039/C5TB00123D, URL http://xlink.rsc.org/?DOI=C5TB00123D.

[89] Wu I, Elisseeff J. Biomaterials and tissue engineering for soft tissue reconstruction. In: Natural and synthetic biomedical polymers. Elsevier; 2014, p. 235–41. http://dx.doi.org/10.1016/B978-0-12-396983-5.00015-6, https://linkinghub.elsevier.com/retrieve/pii/B9780123969835000156.

[90] Darby DR, Cai Z, Mason CR, Pham JT. Modulus and adhesion of Sylgard 184, Solaris, and Ecoflex 00-30 silicone elastomers with varied mixing ratios. J Appl Polym Sci 2022;139(25):1–8. http://dx.doi.org/10.1002/app.52412, URL https://onlinelibrary.wiley.com/doi/10.1002/app.52412.

[91] Ferry JD. Viscoelastic properties of polymers. 3rd ed.. John Wiley & Sons Inc., New York; 1980, p. 672.

[92] Kraus MA, Schuster M, Kuntsche J, Siebert G, Schneider J. Parameter identification methods for visco- and hyperelastic material models. Glass Struct Eng 2017;2(2):147–67. http://dx.doi.org/10.1007/s40940-017-0042-9.